Comments on Inorganic Chemistry
Publication details, including instructions for authors and subscription information:
http://www.informaworld.com/smpp/title~content=t713455155

SECOND-SPHERE TUNING OF THE METAL ION REDUCTION POTENTIALS IN IRON AND MANGANESE SUPEROXIDE DISMUTASES

Laurie E. Grove[a]; Thomas C. Brunold[a]
[a] Department of Chemistry, University of Wisconsin-Madison, Madison, Wisconsin, USA

To cite this Article Grove, Laurie E. and Brunold, Thomas C.(2008) 'SECOND-SPHERE TUNING OF THE METAL ION REDUCTION POTENTIALS IN IRON AND MANGANESE SUPEROXIDE DISMUTASES', Comments on Inorganic Chemistry, 29: 5, 134 — 168
To link to this Article: DOI: 10.1080/02603590802429529
URL: http://dx.doi.org/10.1080/02603590802429529

Comments on Inorganic Chemistry, 29: 134–168, 2008

ISSN: 0260-3594 print
DOI: 10.1080/02603590802429529

Taylor & Francis
Taylor & Francis Group

SECOND-SPHERE TUNING OF THE METAL ION REDUCTION POTENTIALS IN IRON AND MANGANESE SUPEROXIDE DISMUTASES

LAURIE E. GROVE
THOMAS C. BRUNOLD

Department of Chemistry, University of Wisconsin-Madison, Madison, Wisconsin, USA

Iron and manganese superoxide dismutases (Fe- and MnSODs, respectively) are metalloenzymes that catalyze the disproportionation of superoxide to dioxygen and hydrogen peroxide whereby the metal ion cycles between an oxidized and one-electron reduced state. Although Fe- and MnSODs exhibit similar protein and active-site structures, they display strict metal-ion specificities. To understand the origin of this specificity, we performed spectroscopic and computational studies of various FeSOD species and found that certain second-sphere residues exert significant control over the proton-coupled metal ion reduction potential, which must be tuned differently for active site-bound Fe and Mn to permit both substrate oxidation and reduction.

***Keywords*: density functional theory, magnetic circular dichroism spectroscopy, metal ion redox tuning, quantum mechanics/molecular mechanics calculations, superoxide dismutases**

***Abbreviations*: Abs, electronic absorption; Asp, aspartic acid; CD, circular dichroism; COSMO, conductor-like screening model; CT, charge transfer; DFT, density functional theory; EPR, electron paramagnetic resonance; Gln, glutamine; Glu, glutamic acid; His, histidine; INDO/S-CI, intermediate neglect of differential overlap/spectroscopic parameterization-configuration interaction; IP, ionization potential; LF,**

Address correspondence to Thomas C. Brunold, Department of Chemistry, University of Wisconsin-Madison, Madison, WI 53706, USA. E-mail: brunold@chem.wisc.edu

ligand field; LMCT, ligand-to-metal charge transfer; MCD, magnetic circular dichroism; MM, molecular mechanics; MO, molecular orbital; NHE, normal hydrogen electrode; NMR, nuclear magnetic resonance; PA, proton affinity; PDB, protein databank; QM, quantum mechanics; QM/MM, quantum mechanics/molecular mechanics; SOD, superoxide dismutase; Trp, tryptophan; Tyr, tyrosine; WT, wild-type; ZFS, zero-field splitting; ZPE, zero-point energy.

INTRODUCTION

Overview

The structurally similar iron and manganese superoxide dismutases (FeSOD and MnSOD, respectively) are excellent examples from bioinorganic chemistry of outer-sphere tuning of metalloenzyme active-site properties.[1,2] Like the structurally unrelated copper/zinc and nickel superoxide dismutases (Cu/ZnSOD and NiSOD, respectively, see Table 1), Fe- and MnSODs catalyze the disproportionation of the superoxide radical anion, $O_2^{\bullet -}$, into O_2 and H_2O_2.[3–5] Consequently, these enzymes fulfill a vital role in the defense of aerobic and aerotolerant organisms against $O_2^{\bullet -}$, a species that has been implicated in aging and numerous neurodegenerative diseases such as Alzheimer's and Parkinson's diseases.[6–9] Both Fe- and MnSODs are present in the cytosol of prokaryotes, while MnSODs are also found in the mitochondria of eukaryotes. Some bacterial species, such as *Escherichia coli*, possess the genes for both Fe- and MnSODs. These species typically produce just FeSOD under anaerobic conditions, expressing the gene for MnSOD only upon exposure to oxygen (Table 1).[10,11] Fe- and MnSODs have been the subject of extensive kinetic, X-ray crystallographic, spectroscopic, and computational studies. This *Comments* article summarizes the key insights gained in our studies of the mechanism by which second-sphere amino-acid residues differently tune the metal ion reduction potentials in these enzymes.

Structural Characteristics of Fe- and MnSODs

The Fe- and MnSODs display remarkable structural similarities.[12–14] They are typically isolated as homodimers or homotetramers, composed of subunits of $\sim$21 kDa, each containing one metal ion. Each subunit consists of two domains; the N-terminal domain is predominantly composed of two antiparallel α-helices, while the C-terminal domain

Table 1. Characteristics of the four superoxide dismutase classes

Enzyme	Metal ion coordination environment	Metal ion oxidation states	Species
FeSOD	Fe^{3+}: 5-coordinate, trigonal bipyramidal, 3 His, 1 Asp, 1 OH^- Fe^{2+}: 5-coordinate, trigonal bipyramidal, 3 His, 1 Asp, 1 H_2O	$Fe^{3+/2+}$	prokaryotes
MnSOD	Mn^{3+}: 5-coordinate, trigonal bipyramidal, 3 His, 1 Asp, 1 OH^- Mn^{2+}: 5-coordinate, trigonal bipyramidal, 3 His, 1 Asp, 1 H_2O	$Mn^{3+/2+}$	eukaryotes/prokaryotes
Cu/ZnSOD			eukaryotes/prokaryotes
Cu	Cu^{2+}: 4-coordinate, distorted square planar, 4 His Cu^{1+}: 3-coordinate, trigonal planar, 3 His	$Cu^{2+/1+}$	
Zn	Zn^{2+}: 4-coordinate, distorted tetrahedral, 3 His, 1 Asp	Zn^{2+}	
NiSOD	Ni^{3+}: 5-coordinate, square pyramidal, 2 Cys, backbone amide, N-terminal NH_2, 1 His Ni^{2+}: 4-coordinate, square planar, 2 Cys, backbone amide, N-terminal NH_2	$Ni^{3+/2+}$	Streptomyces species/cyanobacteria

possesses a three-layer structure with three-stranded antiparallel β-sheets and 4 additional α-helices (Figure 1a). The metal ion resides at the domain interface and is coordinated by two residues from each domain. Specifically, the metal ion is in a trigonal bipyramidal coordination environment with 2 histidine (His) ligands and an aspartate (Asp) bound equatorially, and a His and solvent molecule bound axially.[15–19] The solvent ligand is an anionic hydroxide and a neutral water molecule in the oxidized (+3) and reduced (+2) states of the enzymes, respectively, and is involved in two hydrogen bonds. It is a hydrogen-bond donor to the non-coordinating oxygen of the Asp ligand and a hydrogen-bond acceptor from a second-sphere glutamine (Gln) residue (Figure 1b). Unlike the first coordination sphere, which is more or less identical for all Fe- and MnSODs studied to date, the positioning of the second-sphere Gln residue varies quite substantially. In the *E. coli* enzymes, this Gln derives from the N-terminal domain (residue 69) in FeSOD, but from the C-terminal domain (residue 146) in MnSOD.[2,20] In both enzymes, Gln has additional hydrogen-bond interactions with Asn, Trp, and Tyr residues, as illustrated in Figure 1b.

Catalytic Mechanisms of Fe- and MnSODs

During catalysis, the metal ion of the Fe- and MnSODs cycles between the 3+ and 2+ states. From kinetic and computational studies[15–17] it is generally believed that metal-ion reduction by $O_2^{\bullet-}$ to yield O_2 (for which the reduction potential $E^\circ = -330$ mV vs. NHE) is accompanied by proton uptake by the active site, while one proton is released in the process of metal-ion oxidation via reduction of $O_2^{\bullet-}$ to H_2O_2 ($E^\circ = 890$ mV vs. NHE) as indicated in Eqs. (1a) and (1b) (where M represents Fe or Mn).[21] Experimental and computational evidence suggests that the solvent ligand is the site of protonation upon metal-ion reduction by substrate, alternating between OH^- and H_2O for the M^{3+} and M^{2+} oxidation states, respectively.[15–19] Redox titrations carried out for Fe- and MnSODs have indicated that the $M^{3+/2+}$ reduction potential is ~20 to 300 mV (vs. NHE) and is therefore adequately tuned for rapid $O_2^{\bullet-}$ reduction and oxidation based on the corresponding $O_2^{\bullet-}$ reduction potentials.[21–23] One noteworthy difference in the mechanisms of Fe- and MnSODs is the observation of a zeroth-order disappearance of $O_2^{\bullet-}$ for MnSOD isolated from several species, including *E. coli*, which was proposed to be indicative for the formation of a reversibly inhibited

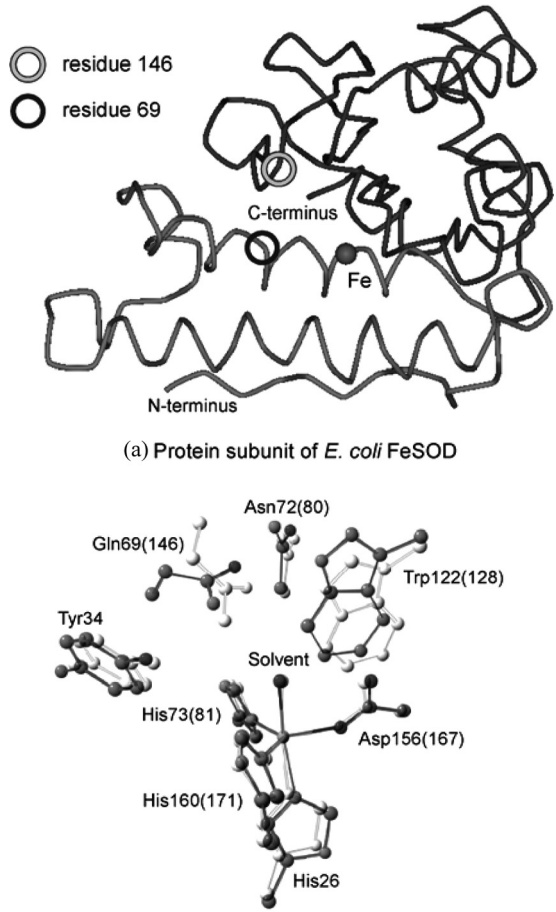

Figure 1. (a) Protein subunit of *E. coli* FeSOD (based on PDB file 1ISA).[2] Domain 1 (N-terminal domain) is shaded as light gray and domain 2 (C-terminal domain) is shaded dark gray. The metal ion represented by a sphere lies at the interface of the two domains. The positions of residues 69 (a Gln in FeSOD) and 146 (the corresponding Gln in MnSOD) are indicated. (b) Superposition of the active-site structures of *E. coli* FeSOD (gray shades) and MnSOD (white monotone). Residue numbers are given for FeSOD and (in parentheses) MnSOD.

form of the enzyme.[15,24–26] This so-called product-inhibited complex exhibits absorption bands at 480 and 650 nm (20 833 and 15 385 cm^{-1}, respectively). Although the structure of this complex has not yet been

definitively determined, a computational analysis of the corresponding electronic absorption spectrum has led to the proposal that it is a (η^2-O_2)-Mn^{3+} species with an axially-bound H_2O ligand.[27]

$$M^{3+}SOD + O_2^{\bullet -} + H^+ \rightarrow M^{2+}SOD(H^+) + O_2 \quad (1a)$$

$$M^{2+}SOD(H^+) + O_2^{\bullet -} + H^+ \rightarrow M^{3+}SOD + H_2O_2 \quad (1b)$$

The second-order rate constants for $O_2^{\bullet -}$ disproportionation by Fe- and MnSODs approach the diffusion-controlled limit, therefore making it virtually impossible to trap reaction intermediates for spectroscopic studies. To overcome this problem, substrate analogues have been used extensively to identify possible substrate-binding sites and modes. In the case of FeSOD, small ions such as fluoride (F^-), azide (N_3^-), and hydroxide (OH^-) have been shown to bind to the Fe^{3+} ion to form 6-coordinate species;[2,28–30] however, only nitric oxide (NO) appears to bind to Fe^{2+} to yield an $\{Fe\text{-}NO\}^7$ complex.[31] Based on these findings, it is widely believed that FeSOD employs an inner-sphere mechanism for substrate oxidation, whereas substrate reduction may occur in the outer-sphere, with a proposed outer-sphere anion (and possibly substrate) binding pocket near the Tyr34 residue (Figure 1b).[16,31] By using an outer-sphere electron-transfer mechanism for substrate reduction, FeSOD may prevent peroxide from accessing the active site and thus minimize the likelihood for protein inactivation due to Fenton-like chemistry.[32,33]

For Mn^{3+}SOD, azide binding to the metal ion has been shown to be temperature-dependent; that is, at low temperatures a 6-coordinate species is observed, while under physiological conditions, the Mn^{3+} ion is predominantly 5-coordinate.[34,35] The ligand that dissociates at higher temperatures was proposed to be the azide anion itself, based on a combined spectroscopic and computational study of this species.[36] Interestingly, the Tyr34 → Phe (Y34F) Mn^{3+}SOD mutant binds azide to form a 6-coordinate species at all temperatures, suggesting that a hydrogen bond between Tyr34 and azide in wild-type (WT) Mn^{3+}SOD may facilitate azide dissociation to yield a 5-coordinate species (or a very weakly ligated 6-coordinate species) at physiological temperatures. By analogy, WT Mn^{3+}SOD may react with substrate to form an outer-sphere, or very weakly bound inner-sphere complex.[36] Lastly, in the case of Mn^{2+}SOD, the enzymes from *E. coli* and *R. capsulatus* have been

shown to form a 6-coordinate species with azide, but not fluoride.[37] Interestingly, Y34F Mn^{2+}SOD binds neither azide nor fluoride, indicating that Tyr34 is strongly involved in regulating anion access to the metal center in both oxidation states.[38]

Metal-Ion Specificity Exhibited by Fe- and MnSODs

Despite the structural similarities inherent to the Fe- and MnSODs, the majority of SODs studied to date display metal-specific activity.[23,39,40] For example, the Fe-substituted MnSOD (Fe(Mn)SOD) and Mn-substituted FeSOD (Mn(Fe)SOD) from *E. coli* display less than 1% of the activity of the WT enzymes. Anion-binding studies have revealed perturbed access to the active-sites in these species,[37,41] thus providing an explanation for modest decreases in activity, but not the loss of more than 99% of WT activity.[23,42–44] A straightforward explanation for the lack of activity of the metal-substituted enzymes was put forward by Miller and coworkers who determined that the metal ion reduction potentials of *E. coli* Fe(Mn)SOD and Mn(Fe)SOD are significantly different from those of their WT counterparts.[23,44] Specifically, the reduction potential of Fe(Mn)SOD was found to be depressed by over 400 mV relative to that of WT FeSOD, while for Mn(Fe)SOD the E° was shown to be elevated by over 500 mV from that of WT MnSOD (Figure 2). These results indicate that the two protein matrices depress the E° of the metal ion by fixed (though distinct) amounts, regardless of whether the active site is occupied by Fe or Mn. As indicated in Figure 2, the (Mn)SOD protein matrix lowers the E° of $Mn^{3+/2+}$ and $Fe^{3+/2+}$ (in MnSOD and Fe(Mn)SOD, respectively) by more than 1 V from the E° of the corresponding hexaquo complexes ($E^\circ = 1510$ and 770 mV vs. NHE for $Mn(H_2O)_6$ and $Fe(H_2O)_6$, respectively), whereas the (Fe)SOD protein matrix depresses the E° of each metal ion by only $\sim$550 mV. The origin of this distinct metal-ion reduction-potential tuning of the (Mn)SOD and (Fe)SOD protein matrices was proposed to lie in the different positioning of the second-sphere Gln residue. In particular, spectroscopic and X-ray crystallographic studies have indicated that the second-sphere Gln residue forms a stronger hydrogen bond with the solvent ligand in MnSOD and Fe(Mn)SOD than in FeSOD and Mn(Fe)SOD.[2,20,45–47]

The second-sphere Gln residue has been the focus of numerous site-directed mutagenesis studies, which have revealed that changing

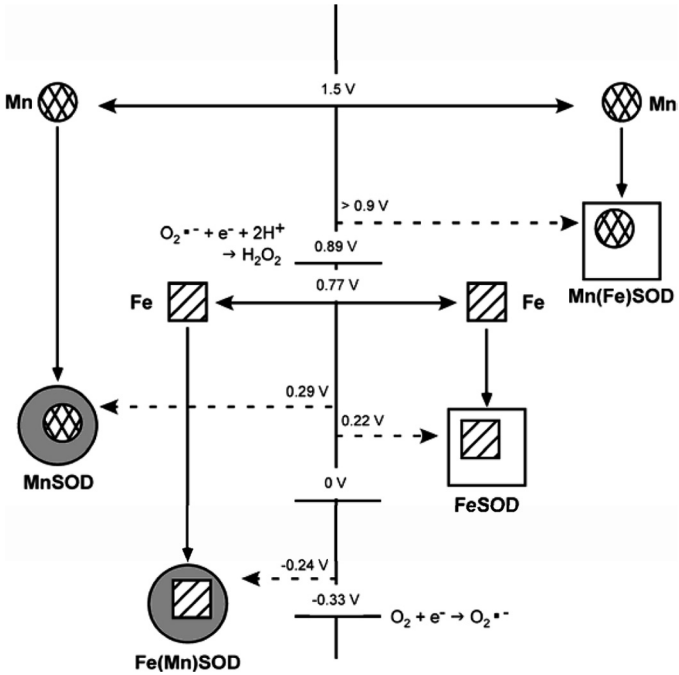

Figure 2. Diagram showing the protein tuning of the metal ion E° in Fe- and MnSODs. The reduction potentials of *E. coli* Fe- and MnSODs are about halfway between the reduction potentials for O_2 and $O_2^{\bullet-}$, while the reduction potentials of Fe(Mn)SOD and Mn(Fe)SOD are de-tuned to such an extent that these species exhibit no measurable activity.

the identity of this residue can also have a significant effect on the metal ion redox properties. For instance, mutation of Gln143 in human MnSOD to either Ala or Asn causes a large stabilization of the Mn^{2+} state.[48,49] Similarly, substitution of Gln69 in *E. coli* FeSOD by a Glu or His results in proteins that are isolated entirely with Fe^{2+} bound or with a mixture of Fe^{2+} and Fe^{3+}, respectively.[50] These mutations are all accompanied by a significant, if not a complete, loss of activity. Substitutions of the second-sphere Gln residue also appear to influence the metal ion binding affinities. For example, in *E. coli* MnSOD the Gln146 → Glu mutation results in a protein that no longer binds Mn.[51] Intriguingly, the Q69G/A141Q and Q77Q/Q146A double mutations in *E. coli* FeSOD and MnSOD, respectively, which effectively change the primary structure position of the Gln in FeSOD to that of the

Gln in MnSOD and vice versa, cause a reversal in the metal ion binding affinities.[52] Similar results were obtained in analogous studies with the corresponding *P. gingivalis* double mutants.[53] Mutations of residues that reside close to the second-sphere Gln, especially those involving the Trp and Tyr residues that hydrogen bond to Gln, have also been shown to influence both the metal ion oxidation state in the as-isolated enzyme and the catalytic activity.[54–56] Presumably, these mutations cause a change in the positioning of the Gln residue and/or a disruption of the proton-transfer pathway from the enzyme active site to the bulk solvent, which likely involves Tyr34 (Figure 1b).

While most Fe- and MnSODs are metal-specific, some species display significant catalytic activity with either metal ion.[57–59] These so-called cambialistic SODs can be classified into two groups based on the identity of the second-sphere residue corresponding to Gln69 in *E. coli* FeSOD. In one group, this residue is a Gln and derives from the N-terminal domain (position 69 using the *E. coli* FeSOD numbering scheme), as in the metal-specific FeSODs.[60] In the second class of cambialistic SODs, this position is instead occupied by a His that derives from the C-terminal domain (position 146 using *E. coli* MnSOD numbering).[61] Interestingly, however, several examples of FeSODs from extremophiles exist that also possess a His residue at this position but nonetheless display metal-specific activity.[62,63] The exact mechanism by which the cambialistic SODs achieve catalytic activity regardless of whether Fe or Mn is bound to their active sites remains largely unexplored.

TECHNIQUES USED FOR STUDYING Fe- AND Mn SUPEROXIDE DISMUTASES

Spectroscopic Methods

A wide range of spectroscopic methods are commonly used in bioinorganic research, e.g., to determine the identity of the active site metal ion, its oxidation state(s), coordination environment, and geometric and electronic structures (Table 2).[64] A particularly sensitive probe of paramagnetic active site metal ions (such as $Fe^{3+/2+}$ and $Mn^{3+/2+}$ bound to SOD active sites) is provided by magnetic circular dichroism (MCD) spectroscopy, which yields information on both the ground-state and excited-state properties.[65,66] When used in conjunction with absorption (Abs) and circular dichroism (CD) spectroscopies, MCD spectroscopy

Table 2. Spectroscopic and computational methods employed in our research of Fe- and MnSODs summarized in this article

Technique	Information content
Spectroscopic Methods	
Electronic absorption (Abs)	Ligand field splittings of metal 3d-based orbitals; relative energies of metal/ligand orbitals
Circular dichroism (CD)	Same as Abs; resolution of Abs bands; nature of transitions
Magnetic CD (MCD)	Same as Abs; resolution of Abs bands; nature of transitions
Variable-temperature variable-field (VTVH) MCD	Spin of ground state; axial (*D*) and rhombic (*E*) zero field splittings (ZFS); polarizations of charge transfer transitions
Computational Methods	
Density functional theory (DFT)	Geometry optimized active-site models; energies of active-site models; electronic structure descriptions; quantitative bonding descriptions
Time-dependent (TD) DFT	Computed transition energies and Abs intensities Validation of active-site models
INDO/S-CI	Same as TD-DFT; computed ground-state properties such as ZFS parameters
Conductor-like screening model (COSMO)	Applied to DFT (or TD-DFT) calculations to account for solvation effects; yields solvation energy corrections for active-site models
Quantum mechanics/molecular mechanics (QM/MM)	Geometry optimizations for large systems (e.g. proteins) by treating active site with QM and protein subunit with MM

offers an almost ideal tool to explore the metal ion geometric and electronic structures, as demonstrated later in this *Comments* article.

For an electronic transition to carry Abs intensity it must be electric dipole allowed; thus, the most intense transitions occur between states of different parity. These so-called Laporte allowed transitions include, among others, charge transfer (CT) excitations that can be categorized as either ligand-to-metal (LMCT) or metal-to-ligand (MLCT). The metal $d \rightarrow d$, or ligand field (LF) transitions, are formally Laporte forbidden; however, there are mechanisms by which this selection rule can be partially relaxed. For example, in distorted ligand environments, as typically found for metalloenzyme active sites, these transitions can gain

intensity via mixing of the LF excited states with higher-energy CT excited states. In CD spectroscopy, a spectrum is obtained by measuring the differential absorption of left and right circularly polarized light, and the CD signal is thus a signed quantity. The selection rules for CD intensity require that the electronic transitions are both electric and magnetic dipole allowed for a given polarization; therefore, only chiral molecules give rise to a CD spectrum. Because LF transitions carry significant magnetic dipole intensity, they can often be observed in a CD spectrum but not in an Abs spectrum, as the latter is dominated by electric dipole allowed CT transitions. By placing the sample in a magnetic field that is applied parallel (or antiparallel) to the propagation axis of the circularly polarized light, an MCD spectrum is obtained. For a transition to carry MCD intensity, it must possess two perpendicular electric dipole transition moments. Since for transition metal complexes of low symmetry, such as enzyme active sites, this requirement can only be met by spin-orbit mixing among excited states, LF transitions often dominate the corresponding MCD spectra. Furthermore, since the magnetic field lifts the ground state spin degeneracy of paramagnetic species, their MCD features show temperature dependence. This temperature dependence can be investigated by carrying out variable-temperature variable-field (VTVH) MCD experiments, in which the MCD signal intensity is measured as a function of magnetic field strength at several different fixed temperatures. An analysis of the VTVH MCD data yields transition polarizations as well as ground state information such as spin-Hamiltonian parameters (Eq. (2), where β is the Bohr magneton, $\mathbf{H}$ is the magnetic field, $\widehat{\mathbf{S}}$ is the spin operator, and D and E are the axial and rhombic zero-field splitting parameters, respectively); this method is particularly useful for integer-spin systems that are difficult to study by electron paramagnetic resonance (EPR) spectroscopy.[67]

$$\widehat{\mathbf{H}} = \mathrm{g}\,\beta\,\mathbf{H}\widehat{\mathbf{S}} + D\left[\widehat{\mathbf{S}}_z^2 - 1/3\ (\mathbf{S}(\mathbf{S}+1))\right] + E\left(\widehat{\mathbf{S}}_x^2 - \widehat{\mathbf{S}}_y^2\right) \qquad (2)$$

Computational Methods

To complement the information gained in spectroscopic studies of metalloenzymes, computational methods can be employed for obtaining additional insight into the active site geometric and electronic structures (Table 2). For transition metal-containing active sites, geometry optimizations are typically performed with density functional theory

(DFT)[68,69] to refine suitably truncated active-site models based on X-ray crystallographic data. These calculations are also extremely useful for generating viable active-site models in cases where structural data are unavailable (e.g., for metal-substituted SODs and short-lived reaction intermediates). While in the last decade gas-phase DFT optimizations on models consisting of only active-site residues have usually been carried out and generally yielded reasonable results, it has recently become more common to utilize approaches that allow the user to treat active-site/protein interactions more rigorously. One method that is particularly appealing to many computational chemists is the combined quantum mechanics/molecular mechanics (QM/MM) methodology, which permits the user to define an active-site region that is treated with high-level QM theory, such as Hartree-Fock (HF) or DFT, while the remainder of the protein is modeled with molecular mechanics (MM).[70–72] Force fields typically used for treating the MM region of proteins include AMBER and CHARMM.[73,74]

Regardless of which computational approach is chosen, it is important to validate the geometry-optimized active-site models on the basis of experimental data. Generally, electronic transition energies and ground-state parameters can be calculated and compared to experimental data to ensure that the active-site models are reasonable. DFT and time-dependent (TD)-DFT calculations are often employed to predict the ground-state properties and Abs spectra, respectively. For certain high-spin complexes, however, such as Fe^{3+}-bound SOD species, TD-DFT often fails to yield reasonable results. In these cases, it may be necessary to resort to other computational approaches, for instance semi-empirical INDO/S-CI calculations.[75,76] Numerous methods also exist to account for solvation (e.g., the conductor-like solvation model (COSMO)),[77,78] which are particularly critical for the calculation of solvation energies and other thermodynamic properties. In the COSMO method, the molecule is treated as if it were situated in a cavity inside a continuum that is an ideal conductor (i.e., the total potential of the system is set to zero); hence, the charge density induced on the surface of the cavity will be approximately equal to the charge density of the solute molecule. The dielectric permittivity value (ε) can be chosen to model the type of solvent (e.g., polar vs. nonpolar) and is used to scale the electrostatic potential obtained from treating the solvent as an ideal conductor to yield a potential that is dependent on ε. To model the electrostatic interactions between the active site and the remainder of

the protein, an ε value of 4 is most commonly used, though it is important to consider a range of ε values, since the exact nature of the protein/active-site interaction can be quite variable.

MECHANISM OF SECOND-SPHERE TUNING OF METAL ION REDUCTION POTENTIALS EMPLOYED BY Fe- AND MnSODs

Proton-coupled reduction potentials can be calculated by summing the energies of the electron-transfer and proton-transfer steps (ε_{ET} and ε_{PT}, respectively, see Eq. (3)). The groundwork for calculating the reduction potentials of superoxide dismutases was laid by Noodleman and coworkers. By using suitably truncated active-site models, these researchers were able to compute proton-coupled reduction potentials that nicely reproduced the trends observed experimentally.[17] To compute the solvation energies for their active-site models, which were obtained by DFT geometry optimizations, they employed the macroscopic electrostatics with atomic detail (MEAD) methodology.[79,80] More recently, Ryde and coworkers,[19,81] along with our group,[82] have reported success in calculating reduction potentials of Fe- and MnSODs using the COSMO approach as implemented in DFT calculations.

$$E^{\circ} = \varepsilon_{ET} + \varepsilon_{PT} \tag{3}$$

Computational Approach for Calculating Metal Ion Reduction Potentials

The methodology developed by Noodleman and coworkers to calculate metal ion reduction potentials employs active-site models derived from X-ray crystallographic data and the MEAD method to account for active site/protein and protein/solvent interactions[83] (see reference 17 for details). As shown in Eq. (3), the electron-transfer and proton-transfer energies are considered separately. The expression for the electron-transfer energy (ε_{ET}, Eq. (4) contains three terms: the gas-phase ionization potential (IP) of the Fe^{2+}- or Mn^{2+}-bound active site models in which the solvent ligand is deprotonated (note that these M^{2+}-OH^{-} species are purely hypothetical), the solvation energy difference ($\Delta\varepsilon_{ET}$) between the reduced and oxidized state models, and a constant of -4.43 V that relates ε_{ET} to the normal hydrogen electrode (NHE).

$$\varepsilon_{ET} = IP + \Delta\varepsilon_{ET} - 4.43 \tag{4}$$

The ε_{PT} of the active-site model is related to the pK of the solvent ligand in the reduced state, which can be expressed as a sum of the gas phase proton affinity (PA) of the hypothetical M^{2+}-OH^- containing active-site model, the difference in solvation energies ($\Delta\varepsilon_{PT}$) of the protonated and deprotonated M^{2+}-bound models, the solvation energy and entropic contribution for a free proton (-268.26 kcal/mol), and the zero-point energy (ZPE) and work term (Eq. (5)).

$$1.37[\mathrm{p}K(\mathrm{M}^{2+}\text{-}\mathrm{OH}_2)] = \mathrm{PA} + \Delta\varepsilon_{PT} - 268.26 + \mathrm{ZPE} + 5/2\ \mathrm{RT} \quad (5)$$

The proton-transfer energy at pH 7 is then computed using Eq. (6).

$$\varepsilon_{PT} = 1.37\{[\mathrm{p}K(\mathrm{M}^{2+}\text{-}\mathrm{OH}_2)] - 7.0\}/23.06 \quad (6)$$

Application to Fe- and MnSODs

Several important results have been obtained from the reduction-potential calculations performed for Fe- and MnSODs by Noodleman and coworkers. First, the number of amino-acid residues included in the active-site models and treated with DFT was shown to dramatically affect the computed values for both ε_{PT} and ε_{ET}. Not surprisingly, for simple $Mn(H_2O)_n$ and $Fe(H_2O)_n$ clusters the calculated pK was found to be dependent on the cluster size, n, approaching the experimental value with increasing values of n.[84] Furthermore, active-site models of MnSOD that only included the metal ion and first-sphere ligands yielded proton-coupled reduction potentials that were more than 1 V lower than the experimental values, despite the fact that the solvation field was suitably accounted for.[85] Including the hydrogen-bond partner Gln in the MnSOD active-site model resulted in a computed proton-coupled reduction potential of $\sim$0.1 V, which is in reasonable agreement with the experimental E° values of 0.26 and 0.31 V for the *B. stearothermophilus* and *E. coli* MnSODs, respectively.[18] Lastly, Noodleman and coworkers explored if their DFT/MEAD approach could reproduce the experimental trend in reduction potentials observed for three different MnSODs; namely, the *T. thermophilus* and human WT and Q143N MnSOD species.[17] Indeed, while the absolute reduction potentials computed for these species were found to deviate from the experimental E° values by $\sim$0.6 V, they nicely reproduced the relative trend (-0.25, -0.29, and -0.11 V vs. 0.40, 0.31, and 0.58 V, respectively).

These results suggest that treating the second-sphere Gln in active-site models of Fe- and MnSODs at the DFT level is essential for predicting accurate trends in proton-coupled reduction potentials; yet, even then the computed E° values may differ by more than 0.5 V from those determined experimentally.

Two important lessons could be learned from these previous studies regarding the effects of solvation on the calculated reduction potentials. First, it was found that the proton-coupled reduction potential exhibits only a very weak dependence on the dielectric constant. By varying ε between 4 and 80, the largest change in computed E° values was 0.11 V (for MnSOD models).[18,85] A similarly weak dependence of the computed E° values on ε was noted by Ryde and coworkers in their DFT/COSMO calculations for Fe- and MnSODs.[19] This finding is not too surprising considering that the overall charge of the enzyme active site does not change between the oxidized and reduced states and, hence, their difference in solvation energies should be very small. Second, the work of Noodleman and coworkers revealed that the computed value for the solvation energy shows little dependence on the level of approximation used; i.e., nearly identical results were obtained by treating the protein environment as a simple dielectric continuum and by explicitly accounting for the electrostatic potential generated by the individual atoms of the entire protein subunit.[18] While both methods were implemented by using the MEAD methodology, the success of the former approach suggests that other calculations that model the solvent and/or protein as a continuum, such as the COSMO, should be well suited for computing proton-coupled reduction potentials as long as the important hydrogen-bond partners within the active site are treated at the DFT level.

Metal-Ion Reduction Potential-Tuning in FeSODs

To explicitly study the role of the *E. coli* second-sphere Gln residue in metal-ion reduction-potential tuning, we carried out combined spectroscopic and computational studies of the *E. coli* FeSOD and Fe(Mn)SOD species, as well as the Gln69 → Glu (Q69E) and Gln69 → His (Q69H) FeSOD mutants (Figure 3). The experimentally obtained $Fe^{3+/2+}$ reduction potentials for these species span an impressively large range of almost 1 V; i.e., Fe(Mn)SOD ($E^\circ = -240$ mV) < WT FeSOD ($E^\circ = 20$–220 mV) < Q69H FeSOD ($E^\circ = 240$ mV) < Q69E FeSOD

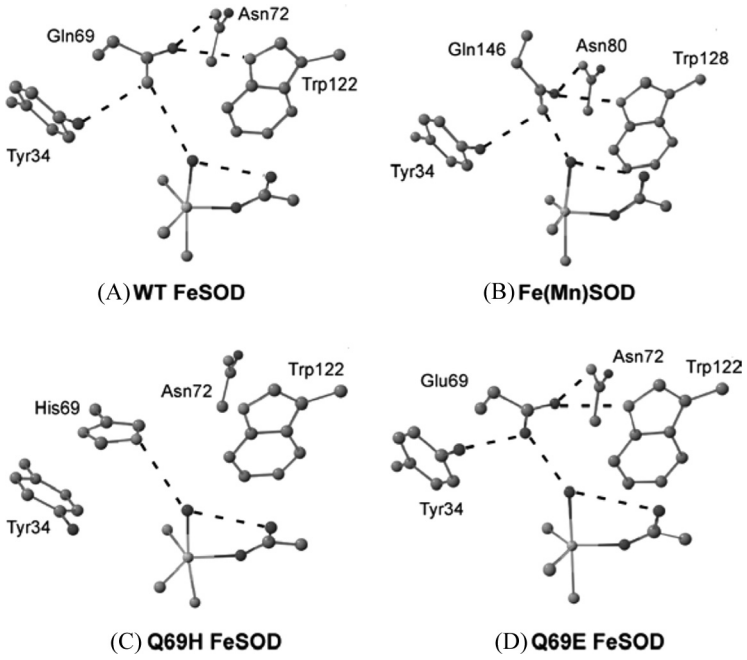

Figure 3. Active-site models derived from X-ray crystallographic data. His ligands are shown as ammonia and amide backbone atoms are omitted for clarity. A) WT FeSOD from PDB file 1ISA; B) Fe(Mn)SOD from PDB file 1MMM; C) Q69H FeSOD from PDB file 1ZA5 and; D) Q69E FeSOD from PDB file 2NYB.[2,46,50,86]

($E^\circ > 660$ mV). As a result, only WT FeSOD and Q69H FeSOD exhibit measurable catalytic activity (Table 3).[44,86] These Fe-bound SOD species provide an excellent set of enzymes for exploring key mechanisms by which the second-sphere residues of Fe- and MnSODs modulate the $M^{3+/2+}$ reduction potentials. First, a comparison of FeSOD and Fe(Mn)SOD provides insight into how the different positioning of the Gln residue contributes to the different metal-ion reduction potentials of these species. Second, the Q69H FeSOD mutant offers a means for investigating the mechanism of metal ion redox tuning in SODs with a naturally occurring second-sphere His residue (such as the cambialistic enzymes and those isolated from extremophiles). Lastly, parallel studies of all four Fe-bound SOD species permit a comparison of the different natures of hydrogen-bonding interactions that occur between the solvent ligand and the three different types of second-sphere residues: a hydrogen-bond donor (Gln), a hydrogen-bond acceptor (Glu), and a residue that

Table 3. Comparison of reduction potentials and specific activities for *E. coli* WT FeSOD, Fe(Mn)SOD, Q69H FeSOD, and Q69E FeSOD[a]

	Specific activity (units/mg)[b]	Reduction potential (mV vs. NHE)	Fe oxidation state in as-isolated enzyme
WT FeSOD	~6000	~20 and 220[c]	3+
Fe(Mn)SOD	0	−240	3+
Q69H FeSOD	1030	260	3+/2+
Q69E FeSOD	3	>660	2+

[a]Adapted from references 44 and 86.

[b]The specific activity corresponds to the extent by which cytochrome c reduction by $O_2^{\bullet-}$ (generated by xanthine/xanthine oxidase system) is inhibited by SOD.[87]

[c]Two separate reduction potential measurements were made for WT FeSOD. The value of 220 mV was obtained by using a procedure similar to that used for Fe(Mn)SOD, while the value of 20 mV was determined by following a procedure similar to that used for Q69H FeSOD.

could be a hydrogen-bond donor or acceptor (His) depending on its protonation state.

Generation of Active-Site Models. X-ray crystallographic data are available for WT FeSOD (in both the Fe^{3+}- and Fe^{2+}-bound states), Fe^{3+}(Mn)SOD (though in this structure the active site is more representative of a 6-coordinate Fe^{3+} species possessing a second OH^- bound trans to Asp167), Q69H FeSOD (containing a mixture of Fe^{3+} and Fe^{2+}), and Q69E Fe^{2+}SOD. These data have revealed several intriguing differences within the second-sphere hydrogen-bond network. For instance, the O(Sol)···N(Gln69/His69) hydrogen-bond distances in FeSOD and Q69H FeSOD are both 3.4 Å, while the analogous O(Sol)···O/N(Glu69/Gln146) hydrogen bonds in Q69E FeSOD and Fe(Mn)SOD are significantly shorter, 2.8 and 2.9 Å, respectively. Because in Q69E Fe^{2+}SOD the Glu69 residue is deprotonated (but becomes protonated in the oxidized state, see below), the drastically shortened O(Sol)···O(Glu69) hydrogen bond has been attributed to the fact that Glu69, a very strong hydrogen-bond *acceptor*, essentially pulls the water ligand toward itself. In contrast, the Gln69 and His69 residues in WT FeSOD and Q69H FeSOD, respectively, are neutral and relatively weak hydrogen-bond *donors* to the solvent ligand. Even

though Gln146 in Fe(Mn)SOD is also neutral and a hydrogen-bond donor, ^{1}H NMR spectroscopic and X-ray crystallographic studies have revealed a short O(Sol)$\cdots$N(Gln146) hydrogen bond in this species, suggesting that the Gln residue is inherently positioned closer to the metal ion in the (Mn)SOD protein matrix than in the (Fe)SOD protein matrix. Consistent with this proposal, a similarly short hydrogen bond was also reported for MnSOD.[20,45,46] Notably, in Q69H FeSOD the His69 residue does not engage in any hydrogen bonds with Tyr, Asn, and Trp, all of which are present in WT FeSOD, Fe(Mn)SOD, and Q69E FeSOD based on X-ray crystallographic data.

To obtain more detailed geometric- and electronic-structure descriptions for the active sites of these four Fe-bound SOD species in both their Fe^{3+} and Fe^{2+} oxidation states, QM/MM geometry optimizations were carried out in which the initial atomic coordinates were based on the X-ray crystallographic data described above. The QM region included the metal ion and all ligands, as well as residue 69 (Gln146 in Fe(Mn)SOD), Tyr34, and Trp122 (Trp128 in Fe(Mn)SOD), while the MM region consisted of the remaining atoms in an entire protein subunit. This approach was shown to yield accurate active-site models on the basis of a comparison between computed and experimental structural and spectral data.[82,88] Throughout the QM/MM geometry optimizations, the 5-coordinate, trigonal bipyramidal coordination environment of Fe was maintained and the optimized metal-ligand bond distances were found to be acceptable based on a comparison to X-ray crystallographic data (if available).[2,46,50,86]

The general structural trends involving the second-sphere residues observed by X-ray crystallography (vide supra) are maintained in the QM/MM-optimized active-site models. Consistent with the experimental data, the most prominent difference between the computational models of the Fe^{3+}- and Fe^{2+}-containing SOD species is the varying degree of conformational freedom provided to the second-sphere Gln (or the analogous His or Glu) residue (Figure 4). For instance, the O(Sol)$\cdots$N(Gln69/146) hydrogen-bond distance increases from 2.86 to 3.56 Å between the Fe^{3+}- and Fe^{2+}-bound states in the FeSOD active-site models but only from 2.77 to 3.03 Å in the Fe(Mn)SOD models, again indicating that the Gln146 in Fe(Mn)SOD is more constrained within the active site. In contrast, the His69 residue in Q69H FeSOD was found to be capable of extensive movement within the active site, since it is no longer constrained by hydrogen bonds to Tyr34, Asn72, and Trp122; hence the O(Sol)$\cdots$N

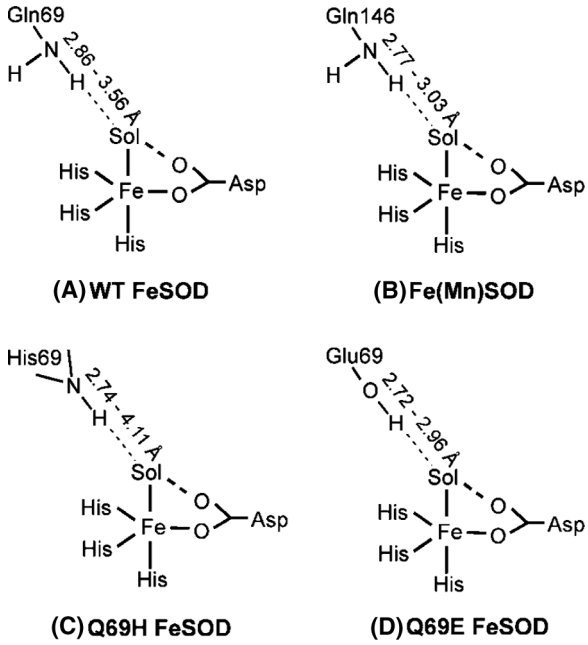

Figure 4. QM/MM-optimized active-site models of (A) WT FeSOD, (B) Fe(Mn)SOD, (C) Q69H FeSOD, and (D) Q69E FeSOD illustrating the change in hydrogen-bond distances between the Fe^{3+}- and Fe^{2+}-bound states. Adapted from references 82 and 88.

(His69) hydrogen bond distance is allowed to vary between 2.74 and 4.11 Å, depending on the nature of the His69 protonation state. Lastly, in the Q69E FeSOD active-site models, the O(Sol)···O(Glu69) hydrogen-bond distances span a narrow range between 2.72 and 2.96 Å, consistent with a strong hydrogen bond between Glu69 and the solvent ligand in both the oxidized and reduced states.

Electronic Structures of Active-Site Models. Oxidized Species. The Abs, CD, and MCD data of WT Fe^{3+}SOD are shown in Figure 5.[30,82] Due to the different selection rules associated with each spectroscopy (vide supra), these spectra contain complementary information about the electronic transition energies and Abs intensities. This information can be extracted by carrying out an iterative fit of the three spectra with the minimal acceptable number of Gaussian bands, as illustrated in Figure 5 (dotted lines). Importantly, the parameters

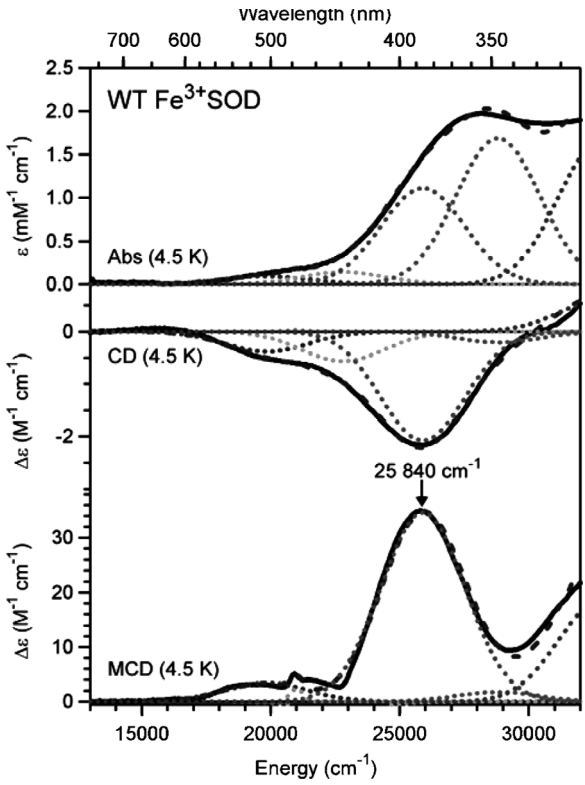

Figure 5. Absorption (top), CD (middle), and MCD (bottom) spectra at 4.5 K of WT Fe^{3+}SOD (solid black line). Individual Gaussian bands (dotted gray lines) and their sums (dashed gray lines) obtained from an iterative fit are shown for each spectrum. Adapted from references 29 and 30.

obtained from fits of the Abs, CD, and MCD spectra for all four Fe^{3+}-bound SOD species investigated were found to be nearly identical.[82,88] In each case the MCD spectrum exhibits weak bands due to spin-forbidden LF transitions below 23000 cm^{-1} and a dominant feature centered at ~26000 cm^{-1} that corresponds to an Asp $\rightarrow$ Fe^{3+} CT transition (Figure 6). Consistent with these experimental findings, the DFT-computed bonding descriptions for these four species are nearly identical in terms of their molecular orbital (MO) compositions and relative energies. The energy splitting calculated for the Fe^{3+} 3d-based MOs is typical of trigonal bipyramidal species. Furthermore, the energy difference between the highest occupied Asp-based MOs and the

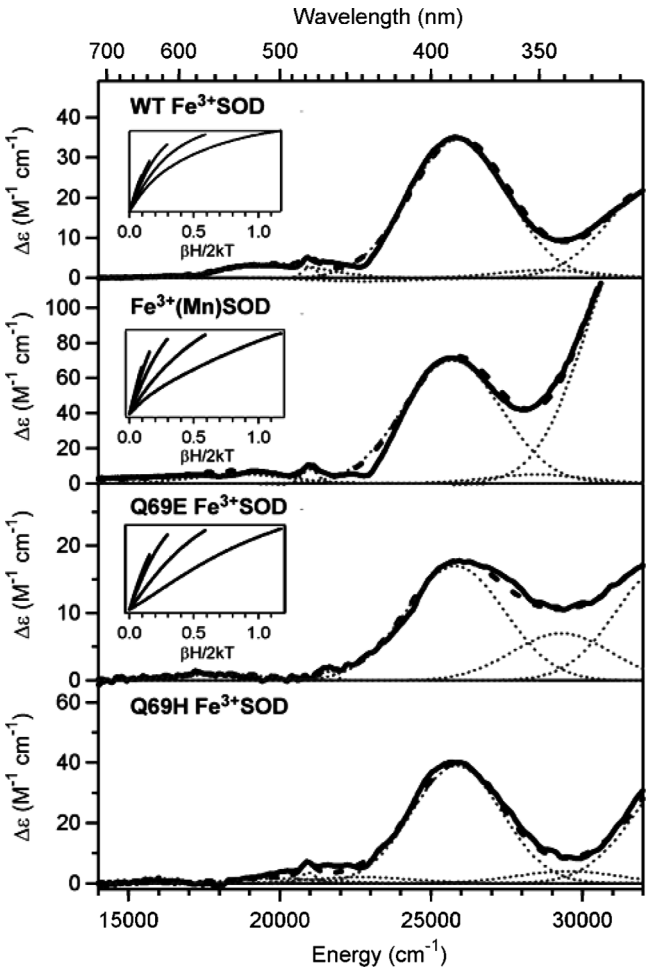

Figure 6. MCD spectra collected at 4.5 K and 7 T of WT Fe^{3+}SOD, Fe^{3+}(Mn)SOD, Q69E Fe^{3+}SOD, and Q69H Fe^{3+}SOD. For each species these data together with the corresponding Abs and CD spectra (not shown) were fit with the minimal acceptable number of Gaussian bands to resolve the major electronic transitions; individual bands are shown by dotted lines and the sum of these bands is shown as dashed lines. Insets: VTVH MCD data for WT Fe^{3+}SOD, Fe^{3+}(Mn)SOD, and Q69E Fe^{3+}SOD. The saturation curves were obtained at 2, 4, 8, 15, and 25 K. Figure adapted from references 82 and 88.

unoccupied Fe 3d-based MOs was found to be nearly identical for the four species, as stipulated by the close resemblance of the corresponding spectroscopic data.

In agreement with X-ray crystallographic data, the nearly identical saturation behavior of the VTVH MCD data obtained for Fe^{3+}SOD, Fe^{3+}(Mn)SOD, and Q69E Fe^{3+}SOD indicates that these species have similar ground-state properties (Figure 6, inset) despite differences within the second coordination sphere.[82] While VTVH MCD data for Q69H Fe^{3+}SOD are not yet available, electron paramagnetic resonance (EPR) data reported for this species are quite similar to those of WT Fe^{3+}SOD, indicating that this species also has a wild-type like metal ion coordination environment.[50] Despite the apparent similarities in metal ion geometric and electronic structures, the Q69E Fe^{3+}SOD and Fe^{3+}(Mn)SOD active sites were found to have a higher affinity for binding a second OH^- trans to Asp at neutral pH to yield 6-coordinate species,[30,46,89] even though their Glu69 and His69 residues, respectively, are neutral like the Gln69 residue in WT Fe^{3+}SOD.[50]

Reduced Species. The MCD spectral data of all four species in their reduced state were also found to be nearly identical. Each MCD spectrum exhibits a single feature centered at $\sim$10 000 cm^{-1},[82,88] which was assigned to the Fe^{2+} $3d_{yz} \rightarrow 3d_{z^2}$ transition. The fact that a single feature is observed near 10 000 cm^{-1} is indicative of a trigonal bipyramidal geometry of the Fe^{2+} ion, consistent with the X-ray crystal structures of WT Fe^{2+}SOD and Q69E Fe^{2+}SOD.[2,50] Even though X-ray crystallographic data are not yet available for Fe^{2+}(Mn)SOD and Q69H Fe^{2+}SOD, the similarity of the corresponding VTVH MCD (Figure 7) and/or ^{1}H NMR spectroscopic data[45,50] to those obtained for WT Fe^{2+}SOD indicates that the metal ion coordination environments are similar in all of the Fe^{2+}-bound SOD species investigated. Finally, similar to the computational results described above for the oxidized enzymes, DFT computations on the QM/MM-optimized Fe^{2+}-bound active-site models did not reveal any significant differences in electronic structure among these four species. In each case the computed LF splittings of the Fe^{2+} 3d-based MOs were found to reflect the trigonal bipyramidal coordination environment of the metal ion.

Calculation of Proton-Coupled Metal Ion Reduction Potentials. The experimental trend in the proton-coupled reduction potentials for WT FeSOD, Fe(Mn)SOD, Q69E FeSOD, and Q69H FeSOD is nicely reproduced by our DFT/COSMO computational results (Table 4), which were obtained by using the QM/MM-optimized active-site models

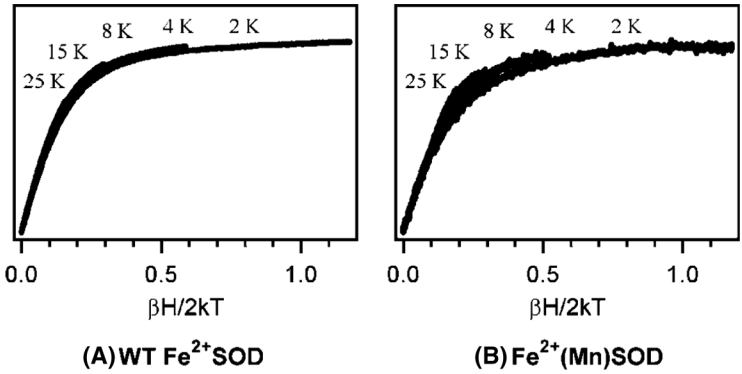

Figure 7. VTVH MCD data collected for WT Fe^{2+} SOD and Fe^{2+}(Mn)SOD at 2, 4, 8, 15, and 25 K. Adapted from reference 82.

and an ε value of 4.0 to account for the effects of solvation (note that in accordance with previous results, the computed solvation energies displayed only a weak dependence on the ε value).[82,88] Importantly, the range of E° values found experimentally for these species is reproduced nearly quantitatively by our computations. Alternatively, parallel DFT/COSMO calculations on active-site models that only included

Table 4. DFT/COSMO-computed proton-coupled metal ion reduction potentials (E° in V vs. NHE) for the QM/MM-optimized active-site models of WT FeSOD, Fe(Mn)SOD, Q69H FeSOD, and Q69E FeSOD

	E° ($\varepsilon = 4.0$)	E° ($\varepsilon = 10.0$)	E° (first-sphere)[a]	E° (exp)[b]
WT FeSOD	0.42	0.39	0.23	0.02–0.22
Fe(Mn)SOD	0.02	−0.02	0.27	−0.24
Q69H FeSOD[c]	0.64, 0.50	0.59, 0.43	0.29, 0.34	0.26
Q69E FeSOD[d]	0.85			>0.66

[a]Computed reduction potentials (with $\varepsilon = 4.0$) for active-site models that only included the first coordination sphere.

[b]Experimental E° values.

[c]The first and second values listed correspond to the reduction potentials calculated for models with the His69 Nδ1 or Nε2 atoms protonated, respectively (paths 1 and 2 in Figure 1.10).

[d]Because of internal proton transfer, the reduction potential computed for this species corresponds to the ε_{ET} value.

the first coordination sphere yielded virtually identical E° values for all four species (Table 4), indicating that the second-sphere amino-acid residues play a vital role in tuning the proton-coupled reduction potential.

For WT FeSOD and Fe(Mn)SOD, the difference in the computed E° values is almost entirely determined by the difference in the ε_{PT} values, as the ε_{ET} values differ by only 0.05 eV (Figure 8). Specifically, the calculated pK of the solvent ligand is nearly 8 pH units lower for Fe^{2+}(Mn)-(Mn)SOD than for WT Fe^{2+}SOD (pK values of 15 and 23, respectively). This increased acidity of the solvent ligand predicted for

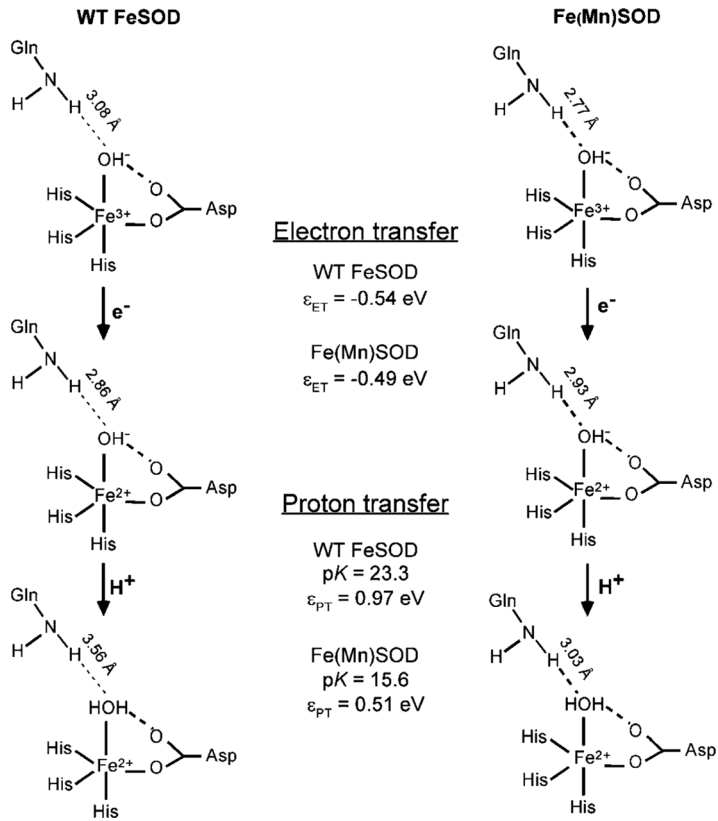

Figure 8. DFT/COSMO computed electron-transfer (ε_{ET}) and proton-transfer (ε_{PT}) energies for the QM/MM geometry-optimized active-site models of WT FeSOD (left) and Fe(Mn)SOD (right).

Fe^{2+}(Mn)SOD can be attributed to the fact that the second-sphere Gln residue (a hydrogen-bond *donor*) is ~ 0.5 Å closer to the metal ion in this species than in WT FeSOD, therefore disfavoring protonation of the solvent ligand and thus $Fe^{3+} \rightarrow Fe^{2+}$ reduction. Similarly, the calculations performed by Noodleman and coworkers on their *E. coli* Fe^{2+}- and Mn^{2+}SOD active-site models have suggested that the pK of the solvent ligand is $\sim$6 pH units higher in the former species, which suggests that the lower pK computed for MnSOD and Fe(Mn)SOD relative to Fe^{2+}SOD is a protein-enforced rather than a metal-specific phenomenon.[17] This proposal that the different metal ion redox tuning in the (Fe)SOD and (Mn)SOD protein matrices largely stems from the different positioning of the second-sphere Gln is entirely consistent with, and provides a straightforward explanation for, the experimental E° values summarized in Figure 2.[23] Note that the increased acidity of the water ligand in Mn^{2+}SOD may also be crucial to minimizing the lifetime of the product-inhibited complex (a putative (η^2-O_2)-Mn^{3+} species), which is governed by the rate of proton transfer to the peroxo moiety to induce product release.[26,90]

Q69E FeSOD is isolated in the reduced state and can only be converted to the Fe^{3+}-bound state by using strong oxidants, such as $KMnO_4$.[86] Consistent with these observations, the computed $Fe^{3+/2+}$ reduction potential for Q69E FeSOD of 0.85 V is more than 400 mV above that predicted for WT FeSOD.[82] Interestingly, the large driving force for the reduction of this species is mainly provided by the deprotonation of

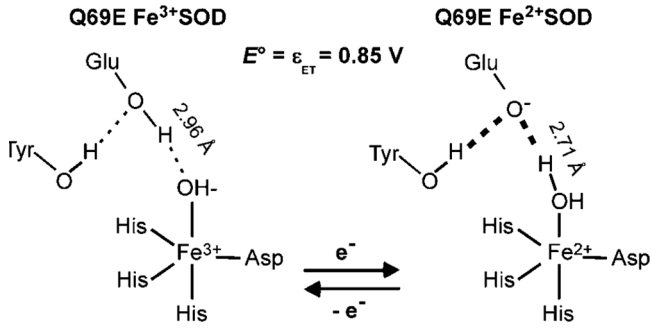

Figure 9. DFT/COSMO computed electron-transfer energy (ε_{ET}) for the QM/MM geometry-optimized active-site models of Q69E FeSOD. Note that in this species internal proton transfer from Glu69 to the solvent ligand occurs upon metal-ion reduction, and the reduction potential is thus equal to the electron transfer energy.

Glu69, as in this case the solvent ligand accepts a proton from this Glu residue, rather than bulk solvent, upon $Fe^{3+} \rightarrow Fe^{2+}$ reduction (Figure 9). The driving force for internal proton transfer by deprotonation of Glu69 is predicted to be 1.79 eV, as compared to 1.0 and 0.51 eV for the external proton transfer in WT FeSOD and Fe(Mn)SOD, respectively. Therefore, Q69E FeSOD provides a textbook example for illustrating how severe the consequences may be of a mutation of a second-sphere residue from a hydrogen-bond donor to a hydrogen-bond acceptor.

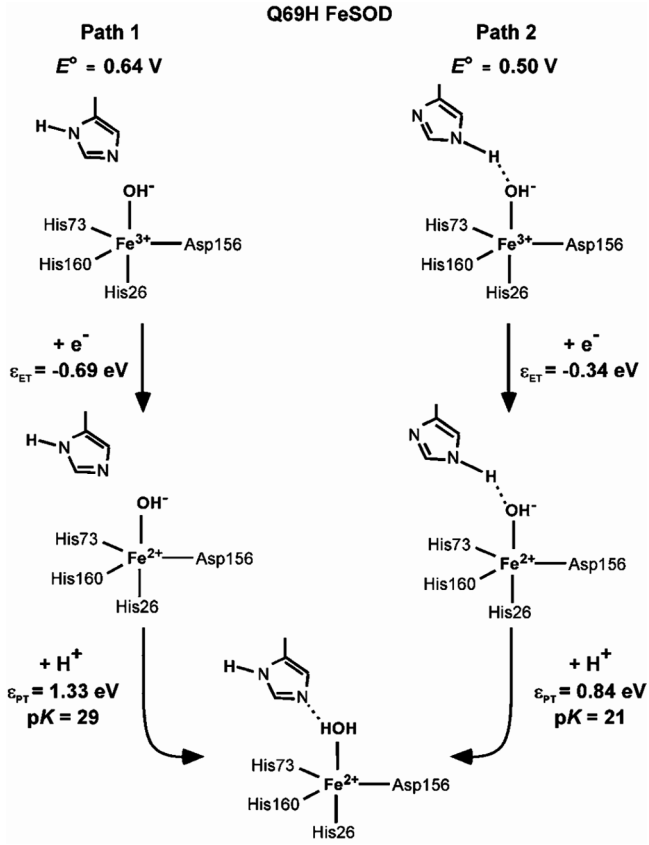

Figure 10. DFT/COSMO computed electron-transfer (ε_{ET}) and proton-transfer (ε_{PT}) energies for the QM/MM geometry-optimized active-site models of Q69H FeSOD. Two pathways are shown: path 1 and path 2 start with the His69 residue protonated at the Nδ1 and Nε2 positions, respectively.

In WT FeSOD, Fe(Mn)SOD, and Q69E FeSOD, movement of the second-sphere Gln or Glu residue is constrained by hydrogen-bond interactions with Tyr34, Asn72, and Trp122 (Figure 3), whereas in Q69H FeSOD, these hydrogen bonds are absent based on both X-ray crystallographic and QM/MM computational studies.[86,88] As a result, our DFT calculations have predicted that the Q69H FeSOD active-site properties are somewhat unique. For instance, the computed electron-transfer energy ε_{ET} for this species differs quite substantially from those obtained for WT FeSOD and Fe(Mn)SOD, by ~ -0.15 or $+0.15$ eV depending on whether the Nδ1 atom or Nε2 atom of His69 is protonated (path 1 and path 2, respectively, in Figure 10). Additionally, because the His69 residue in Q69H FeSOD serves as a weak hydrogen-bond acceptor to the coordinated solvent in the reduced state (a favorable interaction), the computed E° value for this species is more positive than those predicted for FeSOD and Fe(Mn)SOD, consistent with the experimental data summarized in Table 3. The implications of these results for cambialistic SODs possessing a second-sphere His rather than a Gln remain to be explored, as a detailed analysis of the active-site geometric and electronic properties of these species has not yet been performed. An important question to be addressed in future studies of the cambialistic SODs is whether this His residue adopts a different conformation from that observed for Q69H FeSOD, so as to maintain hydrogen bonds to the Asn, Trp, and/or Tyr residues.[61,91] It may even be possible that the His residue adopts different conformations depending on whether Fe or Mn is bound to the active site.

CONCLUSIONS

In recent years, considerable success has been achieved in calculations of the proton-coupled reduction potentials of Fe- and MnSODs, thereby enabling detailed investigations into the origin of the strict metal specificities displayed by these species. By treating the appropriate number of active-site residues with high-level DFT and the remainder of the protein with a lower level of theory, these calculations were found to be reliable in reproducing experimental trends, while the absolute values computed for E° tend to deviate quite substantially from those determined experimentally. Collectively, the calculations described in this *Comments* article have provided compelling evidence that the metal ion redox

tuning in Fe- and MnSODs is accomplished primarily by the second-sphere Gln residue and its ability to either stabilize or destabilize the M^{3+}-OH^- and M^{2+}-OH_2 states via its hydrogen-bond interaction with the solvent ligand. Both experimental and computational data concur that the Gln146 in (Mn)SOD lies closer to the metal ion than the Gln69 in (Fe)SOD, and this difference is the primary reason for the drastically detuned $Fe^{3+/2+}$ and $Mn^{3+/2+}$ reduction potentials observed for Fe(Mn)SOD and Mn(Fe)SOD relative to the WT enzymes (by $\sim$-400 mV and $+$500 mV, respectively). In support of this model, mutations involving this second-sphere Gln can alter the metal ion reduction potential by over 600 mV. Future computational studies aimed at obtaining further insight into the mechanism of metal-ion reduction-potential tuning should also include Mn-bound SOD species, as well as the enigmatic cambialistic SODs, especially those possessing a second-sphere His in place of the Gln residue.

REFERENCES

1. Stallings, W. C., K. A. Pattridge, R. K. Strong, and M. L. Ludwig, 1984. Manganese and iron superoxide dismutases are structural homologs. *J. Biol. Chem.*, **259**, 10695–10699.
2. Lah, M. S., M. M. Dixon, K. A. Pattridge, W. C. Stallings, J. A. Fee, and M. L. Ludwig, 1995. Structure-function in Escherichia-coli iron superoxide-dismutase—Comparisons with the manganese enzyme from *Thermus-thermophilus*. *Biochem.*, **34**, 1646–1660.
3. Miller, A.-F. and D. L. Sorkin, 1997. Superoxide dismutase: A molecular perspective. *Comments Mol. Cell. Biophys.*, **9**, 1–48.
4. Youn, H., E. Kim, J. Roe, Y. C. Hah, and S. Kang, 1996. A novel nickel-containing superoxide dismutase from *Streptomyces spp. Biochem. J.*, **318**, 889–896.
5. Wuerges, J., J.-W. Lee, Y.-I. Yim, H.-S. Yim, S.-O. Kang, and K. D. Carugo, 2004. Crystal structure of nickel-containing superoxide dismutase reveals another type of active site. *Proc. Natl. Acad. Sci. U.S.A.*, **101**, 8569–8574.
6. Valentine, J. S., D. L. Wertz, T. J. Lyons, L. Liou, J. J. Goto, and E. B. Gralla, 1998. The dark side of dioxygen biochemistry. *Curr. Opin. Chem. Biol.*, **2**, 253–262.
7. Culotta, V. C., M. Yang, and T. V. O'Halleron, 2006. Activation of superoxide dismutases: Putting the metal to the pedal. *Biochim. Biophys. Acta.*, **1763**, 747–758.

8. Raha, S. and B. H. Robinson, 2000. Mitochondria, oxygen free radicals, disease and ageing. *Trends Biochem. Sci.*, **25**, 502–508.
9. Simonian, N. A. and J. T. Coyle, 1996. Oxidative stress in neurodegenerative diseases. *Annu. Rev. Pharmacool. Toxicol.*, **36**, 83–106.
10. Nettleton, C. J., C. Bull, C. Baldwin, and J. A. Fee, 1984. Isolation of the *Escherichia coli* iron superoxide dismutase gene: Evidence that intracellular superoxide concentration does not regulate oxygen-dependent synthesis of the manganese superoxide dismutase. *Proc. Natl. Acad. Sci. U.S.A.*, **81**, 4970–4973.
11. Pugh, S. Y. R. and I. Fridovich, 1985. Induction of superoxide dismutases in *Escherichia coli* B by metal chelators. *Journal of Bacteriology*, **162**, 196–202.
12. Yost, F. J. and I. Fridovich, 1973. An iron-containing superoxide dismutase from *Escherichia coli*. *J. Biol. Chem.*, **248**, 4905–4908.
13. Schininà, M. E., L. Maffey, D. Barra, F. Bossa, K. Puget, and A. M. Michelson, 1987. The primary structure of iron superoxide dismutase from *Escherichia coli*. *FEBS Lett.*, **221**, 87–90.
14. Harris, J. I., A. D. Auffret, F. D. Northrop, and J. E. Walker, 1980. Structural comparisons of superoxide dismutases. *Eur. J. Biochem.*, **106**, 297–303.
15. Bull, C., E. C. Niederhoffer, T. Yoshida, and J. A. Fee, 1991. Kinetic-studies of superoxide dismutases—Properties of the manganese-containing protein from *Thermus-thermophilus*. *J. Am. Chem. Soc.*, **113**, 4069–4076.
16. Bull, C. and J. A. Fee, 1985. Steady-state kinetic studies of superoxide dismutases: Properties of the iron containing protein from *Escherichia coli*. *J. Am. Chem. Soc.*, **107**, 3295–3304.
17. Han, W. G., T. Lovell, and L. Noodleman, 2002. Coupled redox potentials in manganese and iron superoxide dismutases from reaction kinetics and density functional/electrostatics calculations. *Inorg. Chem.*, **41**, 205–218.
18. Li, J., C. L. Fisher, R. Konecny, D. Bashford, and L. Noodleman, 1999. Density functional and electrostatic calculations of manganese superoxide dismutase active site complexes in protein environments. *Inorg. Chem.* **38**, 929–939.
19. Rulíšek, L., K. P. Jensen, K. Lundgren, and U. Ryde, 2006. The reaction mechanism of iron and manganese superoxide dismutases studied by theoretical calculations. *J. Comput. Chem.*, **27**, 1398–1410.
20. Edwards, R. A., H. M. Baker, M. M. Whittaker, J. W. Whittaker, G. B. Jameson, and E. N. Baker, 1998. Crystal structure of *Escherichia coli* manganese superoxide dismutase at 2.1-Å resolution. *J. Biol. Inorg. Chem.*, **3**, 161–171.
21. Barrette, W. C., Jr., D. T. Sawyer, J. A. Fee, and K. Asada, 1983. Potentiometric titrations and oxidation-reduction potentials of several iron superoxide dismutases. *Biochem.*, **22**, 624–627.
22. Lawrence, G. D. and D. T. Sawyer, 1979. Potentiometric titrations and oxidation-reduction potentials of manganese and copper-zinc superoxide dismutases. *Biochem.*, **18**, 3045–3050.

23. Vance, C. K. and A.-F. Miller, 2001. Novel insights into the basis for *Escherichia coli* superoxide dismutase's metal ion specificity from Mn-substituted FeSOD and its very high E_m. *Biochem.*, **40**, 13079–13087.
24. McAdam, M. E., R. A. Fox, F. Lavelle, and E. M. Fielden, 1977. A pulse-radiolysis study of the manganese-containing superoxide dismutase from Bacillus stearothermophilus. *Biochem. J.*, **165**, 81–87.
25. Hearn, A. S., C. K. Tu, H. S. Nick, and D. N. Silverman, 1999. Characterization of the product inhibited complex in catalysis by human manganese superoxide dismutase. *J. Biol. Chem.*, **274**, 24457–24460.
26. Abreu, I. A., A. S. Hearn, H. An, H. S. Nick, D. N. Silverman, and D. E. Cabelli, 2008. The kinetic mechanism of manganese-containing superoxide dismutase from *Deinococcus radiodurans*: A specialized enzyme for the elimination of high superoxide concentrations. *Biochem.*, **47**, 2350–2356.
27. Jackson, T. A., A. Karapetian, A.-F. Miller, and T. C. Brunold, 2005. Probing the geometric and electronic structures of the low-temperature azide adduct and the product-inhibited form of the oxidized manganese superoxide dismutase. *Biochem.*, **44**, 1504–1520.
28. Tierney, D. L., J. A. Fee, M. L. Ludwig, and J. E. Penner-Hahn, 1995. X-Ray-absorption spectroscopy of the iron site in Escherichia-coli Fe(III) superoxide-dismutase. *Biochem.*, **34**, 1661–1668.
29. Xie, J., E. Yikilmaz, A.-F. Miller, and T. C. Brunold, 2002. Second-sphere contributions to substrate-analogue binding in iron(III) superoxide dismutase. *J. Am. Chem. Soc.*, **124**, 3769–3774.
30. Jackson, T. A., J. Xie, E. Yikilmaz, A.-F. Miller, and T. C. Brunold, 2002. Spectroscopic and computational studies on iron and manganese superoxide dismutases: Nature of the chemical events associated with active-site pKs. *J. Am. Chem. Soc.*, **124**, 10833–10845.
31. Jackson, T. A., E. Yikilmaz, A.-F. Miller, and T. C. Brunold, 2003. Spectroscopic and computational study of a non-heme iron $\{Fe\text{-}NO\}^7$ system: exploring the geometric and electronic structures of the nitrosyl adduct of iron superoxide dismutase. *J. Am. Chem. Soc.*, **125**, 8348–8363.
32. Yamakura, F. 1984. Destruction of tryptophan residues by hydrogen peroxide in iron-containing superoxide dismutase. *Biochem. Biophys. Res. Commun.*, **122**, 635–641.
33. Beyer, W. F. and I. Fridovich, 1987. Effect of hydrogen peroxide on the iron-containing superoxide dismutase of *Escherichia coli*. *Biochem.*, **26**, 1251–1257.
34. Whittaker, M. M. and J. W. Whittaker, 1997. A "thermophilic shift" in ligand interactions for *Thermus thermophilus* manganese superoxide dismutase. *J. Biol. Inorg. Chem.*, **2**, 667–671.

35. Whittaker, M. M. and J. W. Whittaker, 1996. Low-temperature thermochromism marks a change in coordination for the metal ion in manganese superoxide dismutase. *Biochem.*, **35**, 6762–6770.
36. Jackson, T. A., A. Karapetian, A.-F. Miller, and T. C. Brunold, 2004. Spectroscopic and computational studies of the azide-adduct of manganese superoxide dismutase: Definitive assignment of the ligand responsible for the low-temperature thermochromism. *J. Am. Chem. Soc.*, **126**, 12477–12491.
37. Tabares, L. C., N. Cortez, B. Y. Hiraoka, F. Yamakura, and S. Un, 2006. Effects of substrate analogues and pH on manganese superoxide dismutase. *Biochem.*, **45**, 1919–1929.
38. Tabares, L. C., N. Cortez, and S. Un, 2007. Role of tyrosine-34 in the anion binding equilibria in manganese(II) superoxide dismutases. *Biochem.*, **46**, 9320–9327.
39. Beyer, W. F. and I. Fridovich, 1991. *In vivo* competition between iron and manganese for occupancy of the active site region of the manganese-superoxide dismutase of *Escherichia coli*. *J. Biol. Chem.*, **266**, 303–308.
40. Ose, D. E. and I. Fridovich, 1976. Superoxide dismutase: Reversible removal of manganese and its substitution by cobalt, nickel, or zinc. *J. Biol. Chem.*, **251**, 1217–1218.
41. Sorkin, D. L., C. K. Vance, and A.-F. Miller, 1996. NMR studies of proton donation and metal ion specificity in superoxide dismutase. *Biophys. J.*, **70**, MP365–MP365.
42. Whittaker, M. M. and J. W. Whittaker, 1997. Mutagenesis of a proton linkage pathway in *Escherichia coli* manganese superoxide dismutase. *Biochem.*, **36**, 8923–8931.
43. Miller, A.-F. 2008. Redox tuning over almost 1 V in a structurally conserved active site: Lessons from Fe-containing superoxide dismutase. *Acc. Chem. Res.*, **41**, 501–510.
44. Vance, C. K. and A.-F. Miller, 1998. A simple proposal that can explain the inactivity of metal-substituted superoxide dismutases. *J. Am. Chem. Soc.*, **120**, 461–467.
45. Schwartz, A. L., E. Yikilmaz, C. K. Vance, S. Vathyam, and A.-F. Miller, 2000. Mutational and spectroscopic studies of the significance of the active site Gln to metal ion specificity in superoxide dismutase. *J. Inorg. Biochem.*, **80**, 247–256.
46. Edwards, R. A., M. M. Whittaker, J. W. Whittaker, G. B. Jameson, and E. N. Baker, 1998. Distinct metal environment in Fe-substituted manganese superoxide dismutase provides a structural basis of metal specificity. *J. Am. Chem. Soc.*, **120**, 9684–9685.
47. Yikilmaz, E., J. Xie, T. C. Brunold, and A.-F. Miller, 2002. Hydrogen-bond-mediated tuning of the redox potential of the non-heme Fe site of superoxide dismutase. *J. Am. Chem. Soc.*, **124**, 3482–3483.

48. Leveque, V. J. P., M. E. Stroupe, J. R. Lepock, D. E. Cabelli, J. A. Tainer, H. S. Nick, and D. N. Silverman, 2000. Multiple replacements of glutamine 143 in human manganese superoxide dismutase: Effects on structure, stability, and catalysis. *Biochem.*, **39**, 7131–7137.
49. Hsieh, Y. S., Y. Guan, C. K. Tu, P. J. Bratt, A. Angerhofer, J. R. Lepock, M. J. Hickey, J. A. Tainer, H. S. Nick, and D. N. Silverman, 1998. Probing the active site of human manganese superoxide dismutase: The role of glutamine 143. *Biochem.*, **37**, 4731–4739.
50. Yikilmaz, E., J. Porta, L. E. Grove, A. Vahedi-Faridi, Y. Bronshteyn, T. C. Brunold, G. E. O. Borgstahl, and A.-F. Miller, 2007. How can a single second sphere amino acid change cause reduction midpoint changes of hundreds of mV? *J. Am. Chem. Soc.*, **129**, 9927–9940.
51. Edwards, R. A., M. M. Whittaker, J. W. Whittaker, E. N. Baker, and G. B. Jameson, 2001. Outer sphere mutations perturb metal reactivity in manganese superoxide dismutase. *Biochem.*, **40**, 15–27.
52. Hunter, T., J. V. Bannister, and G. J. Hunter, 2002. Thermostability of manganese- and iron-superoxide dismutases from *Escherichia coli* is determined by the characteristic position of a glutamine residue. *Eur. J. Biochem.*, **269**, 5137–5148.
53. Hiraoka, B. Y., F. Yamakura, S. Sugo, and K. Nakayama, 2000. A change of the metal-specific activity of a cambialistic superoxide dismutase from Porphyromonas gingivalis by a double mutation of Gln-70 to Gly and Ala-142 to Gln. *Biochem. J.*, **345**, 345–350.
54. Yamakura, F., S. Sugio, B. Y. Hiraoka, D. Ohmori, and T. Yokota, 2003. Pronounced conversion of the metal-specific activity of superoxide dismutase from *Porphyromonas gingivalis* by the mutation of a single amino acid (Gly155Thr) located apart from the active site. *Biochem.*, **42**, 10790–10799.
55. Hearn, A. S., M. E. Stroupe, D. E. Cabelli, J. R. Lepock, J. A. Tainer, H. S. Nick, and D. N. Silverman, 2001. Kinetic analysis of product inhibition in human manganese superoxide dismutase. *Biochem.*, **40**, 12051–12058.
56. Greenleaf, W. B., J. J. P. Perry, A. S. Hearn, D. E. Cabelli, J. R. Lepock, M. E. Stroupe, J. A. Tainer, H. S. Nick, and D. N. Silverman, 2004. Role of hydrogen bonding in the active site of human manganese superoxide dismutase. *Biochem.*, **43**, 7038–7045.
57. Martin, M. E., B. R. Byers, M. O. J. Olson, M. L. Salin, J. E. L. Aruneaux, and C. Tolbert, 1986. A *Streptococcus mutans* superoxide dismutase that is active with either manganese or iron as a cofactor. *J. Biol. Chem.*, **261**, 9361–9367.
58. Meier, B., D. Barra, F. Bossa, L. Calabrese, and G. Rotilio, 1982. Synthesis of either Fe- or Mn-superoxide dismutase with an apparently identical protein moiety by an anaerobic bacterium dependent on the metal supplied. *J. Biol. Chem.*, **257**, 13977–13980.

59. Amano, A. S. S., H. Tamagawa, K. Iwakura, S. Tsunasawa, and A. Tsunemitsu, 1990. Characterization of superoxide dismutases purified from either anaerobically maintained or aerated *Bacteroides gingivalis*. *J. Bacter.*, **172**, 1457–1463.
60. Sugio, S., B. Y. Hiraoka, and F. Yamakura, 2000. Crystal structure of cambialistic superoxide dismutase from *Porphyromonas gingivalis*. *Eur. J. Biochem.*, **267**, 3487–3495.
61. Schmidt, M., B. Meier, and F. Parak, 1996. X-ray structure of the cambialistic superoxide dismutase from *Propionibacterium shermanii* active with Fe or Mn. *J. Biol. Inorg. Chem.*, **1**, 532–541.
62. Cooper, J. B., K. McIntyre, M. O. Badasso, S. P. Wood, Y. Zhang, T. R. Garbe, and D. Young, 1995. X-ray structure-analysis of the iron-dependent superoxide-dismutase from *Mycobacterium-tuberculosis* at 2.0 Å resolution reveals novel dimer-dimer interactions. *J. Mol. Biol.*, **246**, 531–544.
63. Knapp, S., S. Kardinahl, N. Hellgren, G. Tibbelin, G. Schäfer, and R. Ladenstein. 1999. Refined crystal structure of a superoxide dismutase from the hyperthermophilic archaeon *Sulfolobus acidocaldarius* at 2.2 Å resolution. *J. Mol. Biol.*, **285**, 689–702.
64. Lehnert, N., S. D. George, and E. I. Solomon, 2001. Recent advances in bioinorganic spectroscopy. *Curr. Opin. Chem. Biol.*, **5**, 176–187.
65. Solomon, E. I. and A. B. P. Lever, 1999. *Inorganic Electronic Structure and Spectroscopy*, Wiley, New York.
66. Johnson, M. J. 2000. CD and MCD spectroscopy. In *Physical Methods in Bioinorganic Chemistry: Spectroscopy and Magnetism*, ed. L. Que Jr., 233–285. University Science Books, Sausilito, CA.
67. Neese, F. and E. I. Solomon, 1999. MCD C-term signs, saturation behavior, and determination of band polarizations in randomly oriented systems with spin $S \geq 1/2$. Application to $S = 1/2$ and $S = 5/2$. *Inorg. Chem.*, **38**, 1847–1865.
68. Cramer, C. J. 2002. Density functional theory, In *Essentials of Computational Chemistry: Theories and Methods*, 233–273. John Wiley and Sons, New York.
69. Ziegler, T. 1991. Approximate density functional theory as a practical tool in molecular energetics and dynamics. *Chem. Rev.*, **91**, 651–667.
70. Orozco, M. and F. J. Luque, 2000. Theoretical methods for the description of the solvent effect in biomolecular systems. *Chem. Rev.*, **100**, 4187–4225.
71. Maseras, F. and K. Morokuma, 1995. IMOMM: A new integrated ab initio + molecular mechanics geometry optimization scheme of equilibrium structures and ransition states. *J. Comput. Chem.*, **16**, 1170–1179.
72. Woo, T. K., L. Cavallo, and T. Ziegler, 1998. Implementation of the IMOMM methodology for performing combined QM/MM molecular dynamics simulations and frequency calculations. *Theor. Chem. Acc.*, **100**, 307–313.

73. Cornell, W. D., R. Cieplak, C. I. Bayly, I. R. Gould, K. M. Merz, Jr., D. M. Ferguson, D. C. Spellmeyer, T. Fox, J. W. Caldwell, and P. A. Kollman, 1995. A second generation force field for the simulation of proteins, nucleic acids, and organic molecules. *J. Am. Chem. Soc.*, **117**, 5179–5197.
74. MacKerell, A. D., D. Bashford, M. Bellott, R. L. Dunbrack, J. D. Evanseck, M. J. Field, S. Fischer, J. Gao, H. Guo, S. Ha, D. Joseph-McCarthy, L. Kuchnir, K. Kuczera, F. T. K. Lau, C. Mattos, S. Michnick, T. Ngo, D. T. Nguyen, B. Prodhom, W. E. Reiher, B. Roux, M. Schlenkrich, J. C. Smith, R. Stote, J. Straub, M. Watanabe, J. Wiorkiewicz-Kuczera, D. Yin, and M. Karplus, 1998. All-atom empirical potential for molecular modeling and dynamics studies of proteins. *J. Phys. Chem. B.*, **102**, 3586–3616.
75. Zerner, M. C., G. H. Loew, R. F. Kirchner, and U. T. Mueller-Westerhof, 1980. An intermediate neglect of differential overlap technique for spectra of transition-metal complexes: Ferrocene. *J. Am. Chem. Soc.*, **102**, 589.
76. Neese, F. 2006. A critical evaluation of DFT, including time-dependent DFT, applied to bioinorganic chemistry. *J. Biol. Inorg. Chem.*, **11**, 702–711.
77. Klamt, A. and G. Schüürmann, 1993. COSMO: A new approach to dielectric screening in solvents with explicit expressions for the screening energy and its gradient. *J. Chem. Soc., Perkin Trans.*, **2**, 799–805.
78. Klamt, A., V. Jonas, T. Bürger, and J. C. W. Lohrenz, 1998. Refinement and parametrization of COSMO-RS. *J. Phys. Chem. A.*, **102**, 5074–5085.
79. Bashford, D. and K. Gerwert, 1992. Electrostatic calculations of the pKa values of ionizable groups in bacteriorhodopsin. *J. Mol. Biol.*, **224**, 473–486.
80. Chen, J. L., L. Noodleman, D. A. Case, and D. Bashford, 1994. Incorporating solvation effects into density functional electronic structure calculations. *J. Phys. Chem.*, **98**, 11059–11068.
81. Rulíšek, L. and U. Ryde, 2006. Structure of reduced and oxidized manganese superoxide dismutase: A combined computational and experimental approach. *J. Phys. Chem. B.*, **110**, 11511–11518.
82. Grove, L. E., J. Xie, E. Yikilmaz, A.-F. Miller, and T. C. Brunold, 2008. Spectroscopic and computational investigation of second-sphere contributions to redox tuning in *Escherichia coli* iron superoxide dismutase. *Inorg. Chem.*, **47**, 3978–3992.
83. Lowell, T., F. Himo, W. G. Han, and L. Noodleman, 2003. Density functional methods applied to metalloenzymes. *Coord. Chem. Rev.*, **238**, 211–232.
84. Li, J., C. L. Fisher, J. L. Chen, D. Bashford, and L. Noodleman, 1996. Calculation of redox potentials and pK(a) values of hydrated transition metal cations by a combined density functional and continuum dielectric theory. *Inorg. Chem.*, **35**, 4694–4702.
85. Fisher, C. L., J. L. Chen, J. Li, D. Bashford, and L. Noodleman, 1996. Density-functional and electrostatic calculations for a model of a manganese

superoxide dismutase active site in aqueous solution. *J. Phys. Chem.*, **100**, 13498–13505.

86. Yikilmaz, E., D. W. Rodgers, and A.-F. Miller, 2006. The crucial importance of chemistry in the structure-function link: Manipulating hydrogen bonding in iron-containing superoxide dismutase. *Biochem.*, **45**, 1151–1161.
87. McCord, J. M. and I. Fridovich, 1969. Superoxide dismutase; an enzymic function for erythrocuprein (hemocuprein). *J. Biol. Chem.*, **244**, 6049–6055.
88. Grove, L. E., E. Yikilmaz, J. Xie, A.-F. Miller, and T. C. Brunold, 2008. Consequences of the Q69H mutation in E. coli iron superoxide dismutase: Spectroscopic and computational insight into active site properties. *Biochemistry*, In preparation.
89. Vance, C. K. and A.-F. Miller, 1998. Spectroscopic comparisons of the pH dependencies of Fe-substituted (Mn)superoxide dismutase and Fe-superoxide dismutase. *Biochemistry*, **37**, 5518–5527.
90. Hsu, J.-L., Y. S. Hsieh, C. K. Tu, D. O'Connor, H. S. Nick, and D. N. Silverman, 1996. Catalytic properties of human manganese superoxide dismutase. *J. Biol. Chem.*, **271**, 17687–17691.
91. Schmidt, M., C. Scherk, O. Iakovleva, H. F. Nolting, B. Meier, and F. Parak, 1998. The structure of the azide coordinated superoxide dismutase of Propionibacterium shermanii investigated by X-ray structure analysis, extended X-ray absorption fine structure, Mössbauer and electron paramagnetic resonance spectroscopy. *Inorg. Chim. Acta.*, **276**, 65–72.